Non-contact ultrasonic detection of angled surface defects

B. Dutton, A.R. Clough, M.H. Rosli, R.S. Edwards

University of Warwick, Coventry, CV4 7AL, UK

r.s.edwards@warwick.ac.uk or b.dutton@warwick.ac.uk

Abstract

Non-destructive testing is an important technique, and improvements are constantly needed. Surface defects in metals are not necessarily confined to orientations normal to the sample surface; however, much of the previous work investigating the interaction of ultrasonic surface waves with surface breaking defects has assumed cracks inclined at 90° to the surface. This paper explores the interaction of Rayleigh waves with cracks which have a wide range of angles and depths relative to the surface, using a non-contact laser generation and detection system. Additional insight is acquired using a 3D model generated using finite element method software. A clear variation of the reflection and transmission coefficients with both crack angle and length is found, in both the out-of-plane and in-plane components. The 3D model is further used to understand the contributions of different wavemodes to B-Scans produced when scanning a sample, to enable understanding of the reflection and transmission behaviour, and help identify angled defects. Knowledge of these effects is essential to correctly gauge the severity of surface cracking.

Keywords: Defect Characterization, SAW, Rayleigh wave, Laser Ultrasound, Ultrasound Modelling
PACS: 43.20 +g, 43.55.Ka, 81.70.Fy

1. Introduction

Surface-breaking cracking is a problem in many industries, with, for example, stress corrosion cracking a particular problem in pipework, and rolling

contact fatigue in rails having the potential to lead to rail breakage [1]. Non-destructive testing (NDT) is essential to monitor such areas and ensure defects are detected and characterised before they become critical. In general, metal samples used for testing and calibration of NDT techniques are produced with defects represented by narrow slots, machined normal to the surface to represent surface breaking cracks, and flat bottomed holes [2–6]. However, real cracks can grow at angles to the surface other than 90°, as is the case for rolling contact fatigue in rails, where cracks typically grow initially at angles of around 25° to the surface [1].

Ultrasound has proven to be a suitable technique for characterising surface cracking, in particular through the use of reflection or transmission of Rayleigh waves, a surface wave with both in-plane and out-of-plane components [5, 7–15]. For slot defects machined normal to the surface, measurements have shown that the transmission of broadband Rayleigh waves can be analysed in the frequency regime and used as a measure of crack length [14, 15]. In the near-field, interesting enhancement effects have been observed with the generation or detection point at the defect [9, 12, 13], with the potential of development to give a high probability of detection (POD). Jian et al. [5] also reported multiple reflections of the Rayleigh wave along the crack length. However, in order to ensure that correct information is being obtained, it is essential to extend investigations to allow for cracks with a wide range of angles as well as depths relative to the surface.

Previous research on angled defects has mainly concentrated on wedges (effectively infinite length cracks) in the context of both NDT and geological research [16, 17]. A variation in the reflection coefficient with angle has been observed, and also in the transmission allong the wedge corner into the other wedge face. This suggests that it is important to calibrate the response of finite-length angled defects. Kinra et al. investigated the behaviour of a narrowband wave incident on several angled defects and observed some angle dependence, but the effects were not exploited [12].

This paper investigates the interaction of Rayleigh waves with cracks having a range of lengths and angles relative to the surface (shown schematically in Figure 1), henceforth referred to as simply angle (θ) and length (d). We concentrate mainly on the far-field behaviour of the results, with the near-field enhancements dealt with in a separate publication [18]. Non-contact ultrasonic methods are used as these simplify the experimental configuration through, for example, removing the need for couplant. We report a mixture of experiments and modelling, to fully understand the behaviour of

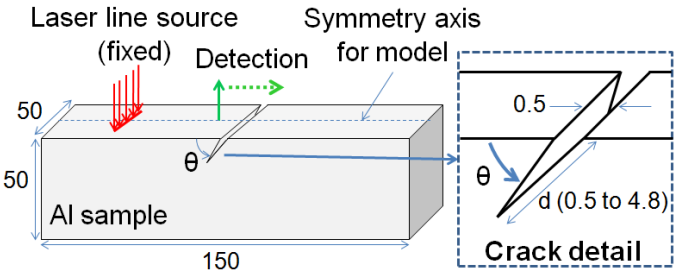

Figure 1: Schematic of a typical sample, showing crack angle (θ, varied from 20° to 170° in the model) and length (d), and scanning arrangement using a fixed laser line source for generation and a scanned detection point. All dimensions in mm.

Rayleigh waves following interactions with surface defects. The out-of-plane (OP) and in-plane (IP) components of the reflection (R) and transmission (T) coefficients are calculated. The resultant is compared to previous analytical models for an infinite length crack [16, 17], while the OP component is compared to experimental measurements for finite length cracks. The behaviour in the region of angled defects is further analysed using B-scans and the calculated wave arrival times for several different wave-modes, highlighting the need for care in the chosen measurement position.

2. Experimental and model details

Figure 1 details the experiment and model set-up. A set of aluminium samples was produced, of dimensions 50x50x150 mm, with a defect across one face, which unlike the model, only one length was used (d = 2mm) and θ varied from 30° to 150°. Defects were machined using laser micromachining to give a v-shape crack with an opening of 500 μm at the top. Experiments were performed using a pulsed Nd:YAG laser line source for generation (1064 nm wavelength and 10 ns pulse duration), filtered to act as a thermoelastic source, and focussed into a line-source of approximate dimensions 6 mm by 300 μm, oriented parallel to the defect. Use of such a line-source enhances surface wave generation in a direction which is perpendicular to the line [19, 20]. When used in the thermoelastic regime this generates primarily through an in-plane shear dipole force, and generates a broadband Rayleigh wave with a centre frequency of approximately 1.67 MHz.

For detection an IOS two-wave mixer laser interferometer detection sys-

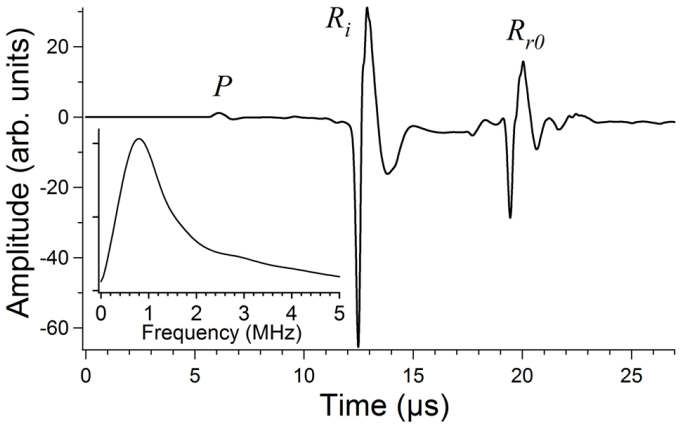

Figure 2: Sample A-scan taken from the model for a 90° crack. The surface skimming longitudinal (P), incident Rayleigh (R_i), and reflected Rayleigh (R_{r0}) waves are clearly visible. The inset shows the FFT of R_i.

tem was used [21]. This is sensitive to the out-of-plane component of the wave motion, and has a bandwidth of 125 MHz with sensitivity from around 100 Hz. Spatial resolution is governed by a combination of the chosen optics and the focus obtained; a spot-size of 200 μm is used here. Surface displacement sensitivity is $4\text{x}10^{-7}$ nm$(\text{W/Hz})^{1/2}$. Its continuous wave laser operates at 1550 nm, with a power variable up to 2 W, dependent on the sample surface quality. Acquired A-scans were averaged 64 times to reduce noise. A significant advantage of this detection system is that the sample surface does not need to be polished, unlike other laser detection systems such as the Michelson interferometer, which requires a mirror-like surface, and samples from polished aluminium through to corroded pipework can be measured.

A 3D model was generated using finite element method (FEM) software, PZFlex [5, 22], using a loading force derived from the experimental laser pulse duration of 10 ns [6, 23], applied onto the sample surface in the form of a dipole to simulate laser line source generation [6, 23]. Appropriate boundary conditions were applied to the model sample, where all surfaces apart from the top were assigned to be 'absorbing' to reduce interference of the Rayleigh wave signals with bulk waves reflected from the sample sides and bottom. All crack surfaces were assigned to be 'free' boundaries. To reduce computation time and memory requirements symmetry was also applied. Additionally, we have investigated a next generation model which applies heat, rather than a force, to the sample, which is similar to the behaviour of a laser when

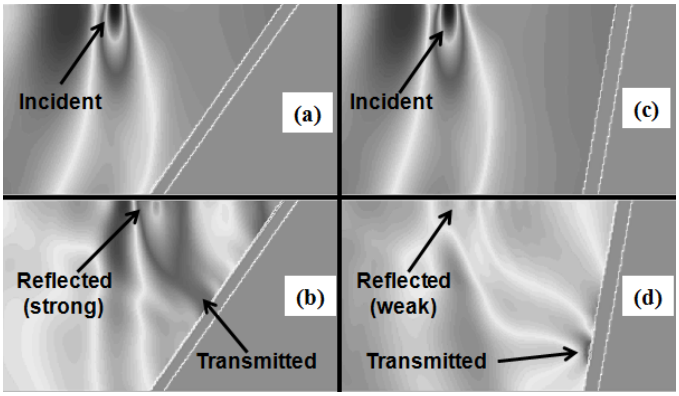

Figure 3: 3D model output of the OP component for a crack of infinite length, showing a slice through the centre of the sample. (a) and (b) show a defect at 55° to the surface, incident, reflected and transmitted, while (c) and (d) show an 80° defect.

used in the thermoelastic regime. This has the advantage of simplifying boundary conditions, in particular when a scanning laser line source is used. An aluminium sample was used, with a Poisson's ratio of 0.35.

Figure 2 shows a sample A-scan output from the model for a 90° crack of length 4 mm, showing the incident Rayleigh wave (R_i) and that reflected from the crack (R_{r0}), plus a surface skimming longitudinal wave (P). The inset shows the fast Fourier transform (FFT) of the windowed Rayleigh wave showing the broadband nature of the pulse. The central frequency (maximum magnitude) for the model and experiments are slightly different, hence throughout this paper the ratio d/λ is used, where λ is the wavelength corresponding to the central frequency. The modelled signals agree very well with experimental results.

3. The influence of a wedge defect on the reflection of Rayleigh waves

The behaviour of Rayleigh waves reflected at a wedge tip (infinite length crack) as a function of wedge angle has been calculated previously using analytical methods [16, 17]. Using the 3D model presented here it is possible to investigate the displacements throughout the material, and build a picture of the propagation of the ultrasound. Figure 3 shows the out-of-plane component of the ultrasonic waves just before (a and c) and just after (b and d) reflection and transmission of the Rayleigh wave at the corner of a wedge

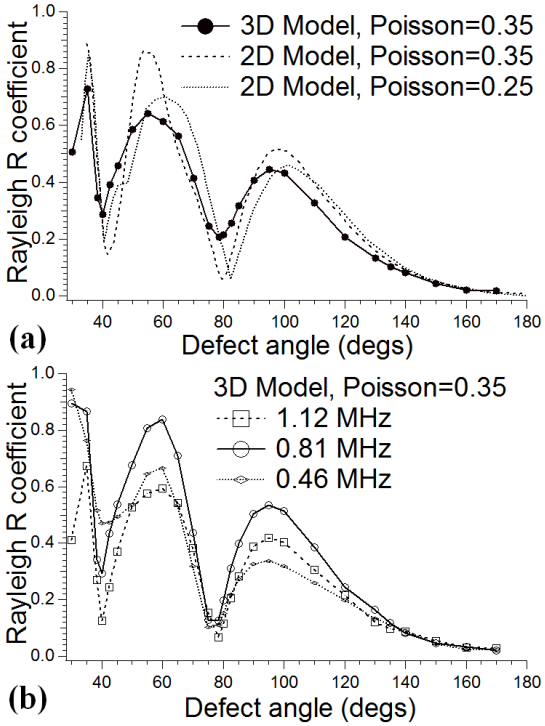

Figure 4: Models for the reflection coefficient from wedges with different wedge angles. (a) solid line: 3D laser generation model for Poisson's ratio of 0.35; dashed line, 2D model for Poisson's ratio of 0.35 [17]; dotted line, 2D model for 0.25 [16]. (b) $R(\nu)$for the 3D model for Poisson's ratio of 0.35 calculated from Equation 1 for several frequencies.

defect, where reflected wave travels allong top surface and transmitted wave allong crack length, for wedges of angle 55° or 80° (note that out-of-plane is defined relative to the top surface of the sample). It is clear that the behaviour of the wave following interaction with the defect has significant angle dependence, and this will have the effect of a variation of the reflection coefficient with angle, as has been observed previously [16, 17]. Very similar behaviour is observed in the IP component.

In previous work dealing with infinite length cracks (wedges), the reflection coefficient was defined as the ratio of the reflected and incident Rayleigh waves, while transmission was calculated using waves which had been transmitted from top surface onto the angled face, for a narrowband signal [16, 17]. Figure 4(a) shows a comparison between the reflection coefficients calculated using 2D analytical methods for Poisson's ratios of 0.25 (dotted lines, from

[16]) and 0.35 (dashed lines, from [17]), and from this 3D model (solid lines and points, Poisson's ratio 0.35). The reflection (R) and transmission (T) coefficients are calculated by comparing the amplitudes of the incident (A_{Ri}), reflected (A_{Rr0}) and transmitted (A_{Rt0}) Rayleigh waves, measured at a fixed ($> 3\lambda$) distance from the crack, with $R = A_{Rr0}/A_{Ri}$ and $T = A_{Rt0}/A_{Ri}$ [5]. Waves were treated as plane waves, due to the use of a line source and the limited distance over which the waves propagate [10]. The reflection coefficients from this and previous work show similar behaviour, with a small angular shift and an apparent smoothing of the behaviour in the 3D model. An oscillating pattern is seen, as expected; for comparison see Figure 3 for the behaviour for a maximum (55°) and minimum (80°) reflection coefficient.

For laser generation the incident and reflected waves are broadband, and hence this method will average over the contributions from different frequencies. Equation 1 describes the method for calculating the reflection coefficient at a single frequency ($R(\nu)$) by comparing the FFTs for the reflected (R_{r0}) and incident (R_i) Rayleigh waves [5].

$$R(\nu) = \frac{FFT[R_{r0}](\nu)}{FFT[R_i](\nu)} \tag{1}$$

Results for $R(\nu)$ at three different frequencies as a function of wedge angle are shown in figure 4(b). The differences between the the current model and previous analytical models observed in Figure 4(a) can therefore be understood through knowledge of the exact frequencies used. Discrepancies are observed for very small angles, where the wedge is becoming critically thin [17], and these will be investigated in more detail when considering the near-field behaviour [18].

4. Calculation of reflection and transmission coefficients for finite length cracks

To simulate more realistic cracking and measurements we consider a finite length crack (Figure 1), and define transmission as that transmitted underneath the crack and reaching the top surface of the sample a certain distance on the other side of the crack [12, 14, 15]. This defines transmission similar to that which can be measured in a potential testing situation for finite length cracks, rather than the definition used in wedge models. The reflection and transmission coefficients will be a function of both θ and d.

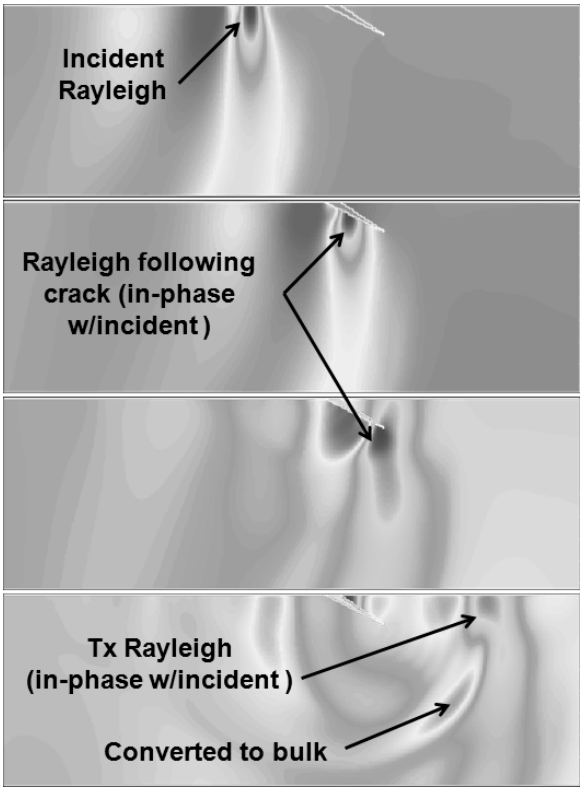

Figure 5: 3D model output for a 150° crack with $d/\lambda = 0.55$, showing the OP component. This shows the propagation of the Rayleigh wave along the crack and mode conversion at the crack bottom.

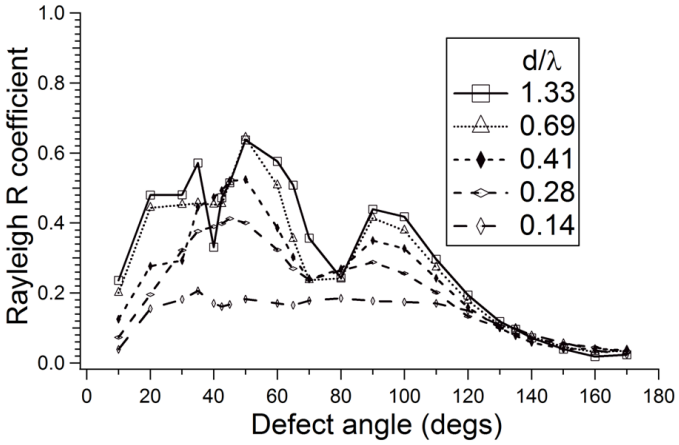

Figure 6: Reflection coefficients for increasing normalised crack lengths from 0.14 to 1.33, showing a general increase of reflection coefficient as d/λ increases.

4.1. Calculation of reflection coefficient

The 3D FEM model was extended to investigate Rayleigh reflection and transmission coefficients for a wide range of angles (10° to 170°) and normalised crack lengths (d/λ of 0.14 to 1.33), where d is kept constant as the crack angle is changed and λ is taken as the central frequency in the broadband pulse. Figure 5 shows a sample 3D model output for the OP component for a Rayleigh wave incident on a 150° crack of $d/\lambda = 0.55$, showing the effect an obtuse angle has on both transmission and reflection. Note that the amplitude is scaled to the maximum and minimum for each part of the figure. Figure 6 shows the modelled reflection coefficients as both angle and crack length are changed. In general, away from the minima, the reflection coefficient increases with d/λ. The oscillating pattern observed in Figure 4 is again found, becoming more prominent with increasing length.

The energy of a Rayleigh wave is concentrated mainly within one wavelength of the sample surface. For small values of d/λ, the majority of the broadband wave will be transmitted underneath the crack, hence the effect of an angled defect will be minimal as only higher frequencies will be affected. However, as the crack length is increased, less is able to be transmitted, and the behaviour will gradually approach that of $d/\lambda = \infty$. Hence, both angle and length need to be considered when explaining reflection coefficients of Rayleigh waves.

For all depths the reflection coefficient for large obtuse angles is very

small, as the wave is primarily transmitted along the crack (see Figure 5). A significant amount of the energy is mode converted into bulk waves at the bottom edge which pass into the bulk of the sample.

4.2. Calculation of transmission coefficient

Similarly, transmission coefficients for the same angle and normalised length ranges were explored through modelling and experiments. Again, both were set up as in Figure 1, with the transmission coefficient measured more than three wavelengths past the crack opening. Figure 7(b) shows peak to peak amplitude of the Rayleigh wave, windowed over the expected arrival time, is measured and plotted as a function of separation between the generation and detection points. As the separation is increased the wave is attenuated, leading to a drop in amplitude, and this must be taken into account when calculating the transmission. However, the drop in signal as the crack blocks some of the wave is clear [15]. This same figure shows two line traces, one for transmitted and a second for incident amplitudes and the ratio of the last points was used to calculate transmission coefficient. Some variation in transmission is seen as different wavemodes reach the surface after mode conversion and transmission (see section 6). However, the surface displacement recovers in the far-field to a stable value.

Figure 7(a) shows the calculated transmission coefficients for different angles and crack lengths; a decrease of transmission coefficient as the length increases is clearly visible, as expected. Part (c) shows the calibrated change in transmission with d/λ from the model for a crack of $\theta = 90°$, in very good agreement with the calibration using broadband EMATs reported in [15]. There is a variation in transmission with angle which must be considered when comparing results from real defects with calibrations based on slots which are machined normal to the surface.

From Figure 7(c), for $\theta = 90°$, the transmission with increasing length follows approximately an exponential decay of $T = \exp[-(d/\lambda\tau)]$, where $\tau = 0.298$ from the fit. Given the penetration of a Rayleigh wave it can be assumed that the transmission will be dominated by the vertical depth into the sample, which varies as $d \sin\theta$. The curves in Figure 7(a) show a fit to $T = \exp[-(d \sin\theta)/\lambda\tau]$, where $\tau = 0.298$ is a constant of the fit; it is clear that this explains some of the angular dependence, however there is still some further dependence, and care must be taken when choosing the detection position relative to the crack at which to measure. When combined with the significant effect of the angle on the reflection coefficient, this small

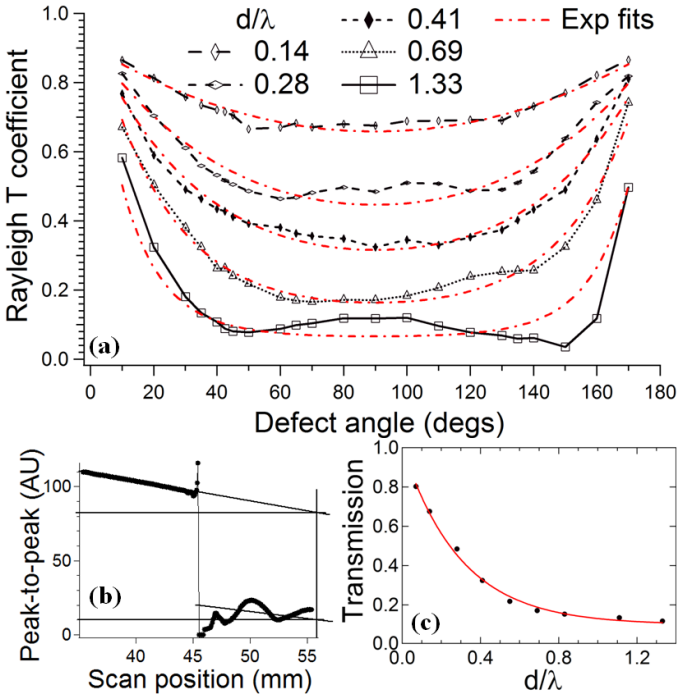

Figure 7: (a) Transmission coefficients for increasing d/λ, showing a regular decrease of transmission as d/λ increases. (b) Rayleigh peak-to-peak amplitude vs. scan position for d/λ = 1.11 and 140° crack. (c) Transmission with length for $\theta = 90°$.

angle dependence has the potential for being exploited for crack angle and depth characterisation, and is the focus of current research.

The term defined as $[1-(R^2+T^2)]$, which has previously been referred to as scattering cross-section [12] or tip-diffraction loss, describes the amount of energy that is absorbed or diffracted into the material through mode conversion. This must always be less than one, and this is the case for all angles measured.

5. Comparison of experiment and model results

Both OP and IP components have been calculated in the model and combined to form the above results. However, as the experiment is sensitive to OP displacements only we now compare just the OP reflection and transmission coefficients. Figure 8 shows the (a) reflection and (b) transmission coefficients from the model (solid lines) and experiments (dashed lines), for a crack length to central wavelength ratio of $d/\lambda = 1.11$. Experimental samples were limited to having minimum and maximum angles of 30° and 150° due to manufacturing limitations; nevertheless, within this range of angles, the behaviour of the reflection and transmission coefficients are in very good agreement. In this case, coefficients consider the full broadband nature of the waves, with some small discrepancies due to the slightly differing frequency ranges. Modelled results are also in very good agreement with results reported in Kinra [12], which used similar crack geometry but a narrowband source, for d/λ values of around 1.33, 1.11 and 0.69.

To compare IP components we would require a different detection technique. IP detection is possible using laser detection techniques such as knife-edge interferometry [24]. Another non-contact technique is the electromagnetic acoustic transducer (EMAT) [25], which can be optimised to measure primarily either the IP or OP component of the velocity [26], but measure velocity rather than displacement. Experiments using such EMATs is ongoing.

6. Optimising measurements of R and T

As can be seen in Figure 7(b), it is important to be careful with the position at which transmission coefficients are measured. The peak-to-peak measurements suggest that different wavemodes reflected and mode-converted

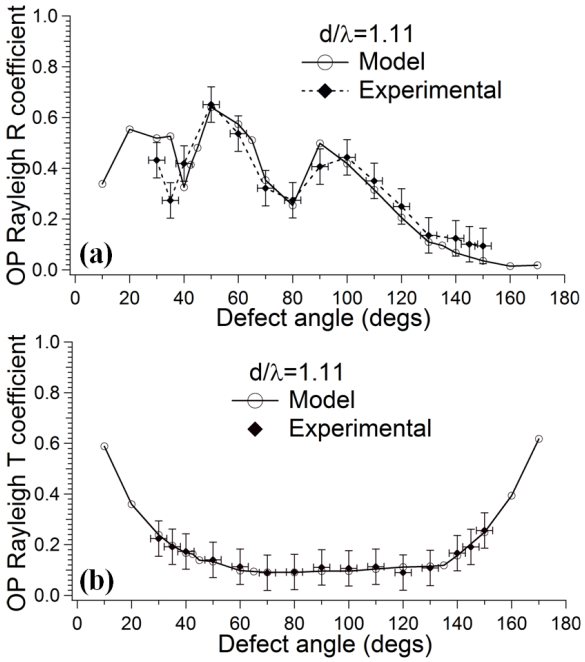

Figure 8: Model and experimental data for laser generation for d/λ = 1.11; (a) OP reflection coefficient, (b) OP transmission coefficient.

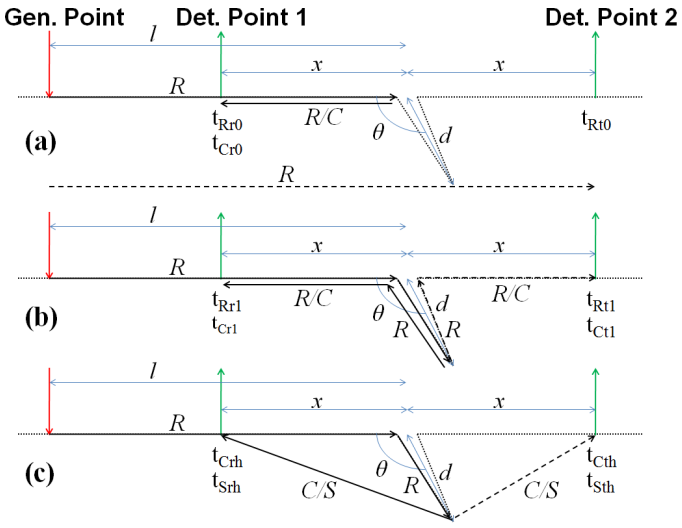

Figure 9: (a) to (c) show schematic reflected, transmitted and mode-converted waves, following [5] but considering angle dependence of the wave paths. Wave velocities are taken to be $v_R = 2940\ ms^{-1}$, $v_C = 6300\ ms^{-1}$, and $v_S = 3110\ ms^{-1}$.

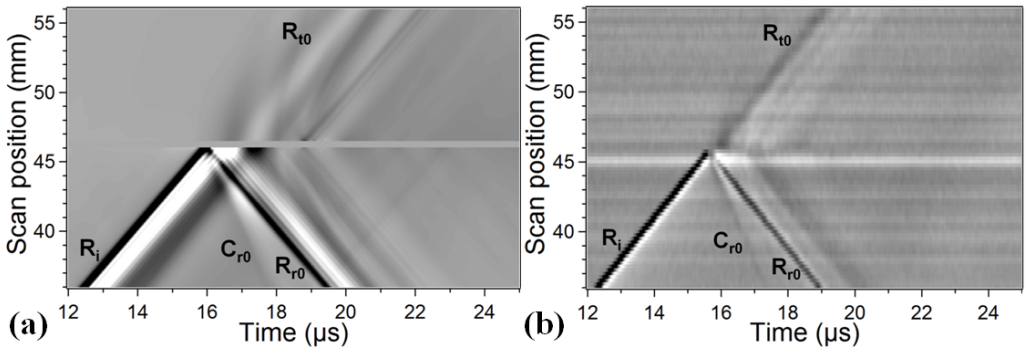

Figure 10: OP B-scan of a 90° crack of d/λ = 1.11 (a) generated from a 3D FEM model, and (b) from experimental measurements.

from the crack are interfering with the windowed Rayleigh wave at certain points.

Figure 10 shows B-scans produced during scanning of a sample with a 90° defect, for (a) modelled and (b) experimental data. These B-scans are comprised of A-scans, such as in Figure 2, for different detection positions, stacked on their side with the amplitude shown by the brightness of the plot. As the distance between generation and detection point (y-axis) is increased the arrival time of the incident Rayleigh wave changes. In both parts of this figure the incident (R_i) and reflected (R_{r0}) Rayleigh waves are clear, as is the transmitted (R_{t0}) wave, which recovers some distance after the defect. The mode-converted surface skimming longitudinal mode (C_{r0}) and the first echoes of the wave up and down the crack are also seen. Interference between waves in the near-field is clear.

Scattering from a 90° crack in a 2D model has been studied previously with the arrival times of different reflected modes calculated [5]. For angled defects, the expected arrival times must be modified to take into account the angle dependence of the wave path. In the following, x is defined to be the distance from the crack to the detection point, taken to always be positive (see Figure 9). The velocities of the Rayleigh, longitudinal and shear waves are v_R, v_C and v_S respectively. A subscript of r describes a reflected wave, while t concerns one which has been transmitted, and d and l are as defined in Figure 9. A Rayleigh wave incident on a crack can be reflected up and down the crack before being reflected or transmitted, and this is described by Equation 2;

$$t_{Rrk} = t_{Rtk} = (l + x + 2kd)/v_R \tag{2}$$

where k is an integer ≥ 0. For transmission, the wave with $k = 0$ corresponds to a low frequency Rayleigh wave which penetrates into the sample and is able to pass directly underneath the crack. Mode conversion is also possible at the crack opening, generating a surface skimming longitudinal wave;

$$t_{Crk} = t_{Ctk} = (l + 2kd)/v_R + x/v_C \tag{3}$$

These correspond to Figures 9(a) and (b).

Equations 4 to 7 correspond to the situation in Figure 9(c); in this case, waves are mode converted to shear (S) or longitudinal (C) waves at the bottom of the crack and propagate into the sample, with a proportion reaching the surface. Here, h denotes a mode converted bulk wave at the bottom of the crack.

$$t_{Crh} = (l + d)/v_R + \sqrt{(x^2 + d^2 - 2xdcos\theta)}/v_C \tag{4}$$
$$t_{Srh} = (l + d)/v_R + \sqrt{(x^2 + d^2 - 2xdcos\theta)}/v_S \tag{5}$$
$$t_{Cth} = (l + d)/v_R + \sqrt{(x^2 + d^2 + 2xdcos\theta)}/v_C \tag{6}$$
$$t_{Sth} = (l + d)/v_R + \sqrt{(x^2 + d^2 + 2xdcos\theta)}/v_S \tag{7}$$

As can be seen from Figure 9, these will have angle dependence, and will reduce to those given in [5] for $\theta = 90°$. It is expected that wavemodes from Equations 2 to 7 will dominate the B-Scan and interference patterns observed in the peak-to-peak measurements.

Following on from Equation 2 for $k = 0$, corresponding to a low frequency Rayleigh wave, a further set of low frequency wavemodes may be observed weakly in the B-Scan. These are waves which have been mode-converted from Rayleigh waves at the bottom of the crack.

$$\begin{aligned}
t_{Crg} &= (l - d\cos\theta)/v_R + \sqrt{(x^2 + d^2 - 2xdcos\theta)}/v_C \\
t_{Ctg} &= (l - d\cos\theta)/v_R + \sqrt{(x^2 + d^2 + 2xdcos\theta)}/v_C \\
t_{Srg} &= (l - d\cos\theta)/v_R + \sqrt{(x^2 + d^2 - 2xdcos\theta)}/v_S \\
t_{Stg} &= (l - d\cos\theta)/v_R + \sqrt{(x^2 + d^2 + 2xdcos\theta)}/v_S
\end{aligned} \tag{8}$$

The expected arrival times of these waves for increasing separation between generation and detection points have been calculated and compared to the B-Scans generated by the model for crack angles of 40°, 50°, 80°, 90°

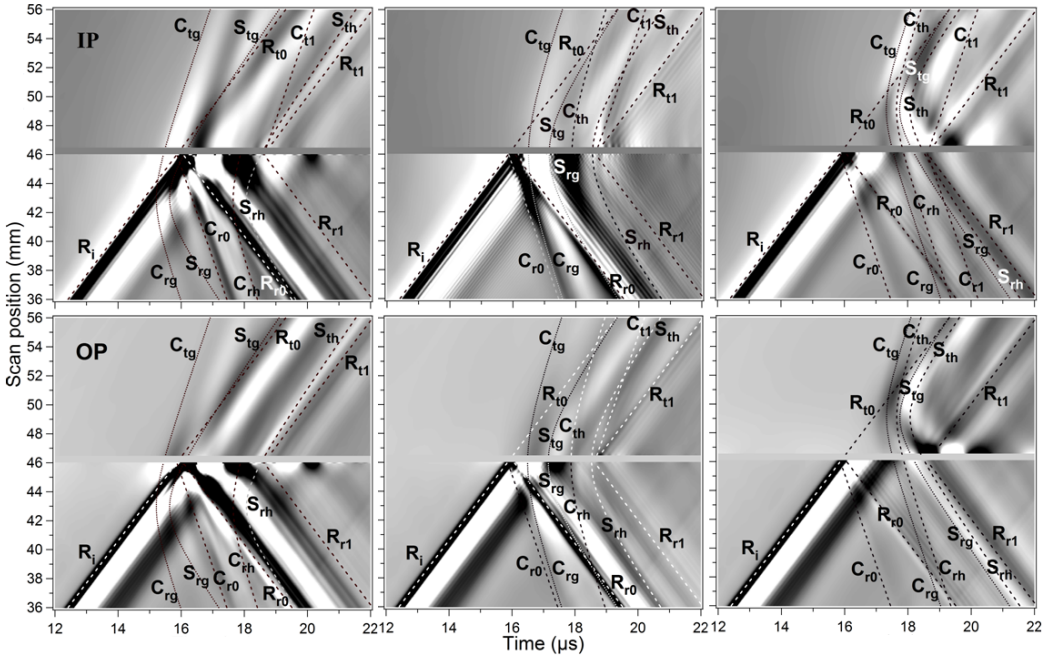

Figure 11: Transmitted (top) and reflected and incident (bottom) waves for angles of (a) 40°, (b) 90° and (c) 140°.

and 140° for 4 mm deep cracks. Figure 11 shows several of these B-Scans for both IP (top) and OP (bottom) components. On each of these figures the dominant wavemodes are clear, as is the interference of waves as their arrival times coincide.

The angle dependence is seen clearly in the arrival times, particularly for modes such as C_{tg}, which for some angles arrives earlier than the low frequency transmitted Rayleigh wave. For $\theta = 40°$, this has an early arrival and interferes with R_{t0} close to the crack, whereas for 140° the interference occurs further away. A further effect of this angular dependence is a change in symmetry of the modes between reflection and transmission. For 90°, the modes with angular dependence are obviously symmetric around the crack. However, for 140° in particular the minimum arrival time for the S_{th} etc. modes are far from the defect. The recovery time, after which the Rayleigh wave amplitude is again significant, will necessarily depend on crack length. However, this work also shows that angle plays a part, and for an equal length crack the recovery time will be greater for the obtuse angle.

Further insight can be gained from the amplitude and frequency content of the reflected and transmitted waves. As expected, R_{r0} is clearer for 40° than for 140°. However, the frequency contents are different. Comparing R_{t0} and R_{t1} again confirms the low frequencies pass underneath the crack, while higher frequencies which are transmitted are more likely to have travelled allong the crack faces. Some differences in the waves observed can be seen between the IP and OP scans. This can be understood by considering the directions of wave travel and wave motion for bulk waves which have reached the surface and are detected by the model. For both IP and OP, the variation in the peak to peak amplitude as the separation is varied seen in Figure 7(b) can be understood by looking at the interference of different waves.

The differences in the B-Scans for different angles offers several interesting possibilities for characterising surface defects. For example, the peak to peak amplitude of the time window for the calculated Rayleigh wave arrival time will vary in the near-field following the crack, depending on the angle. Here, for 40° the window will contain C_{tg} immediately following the crack, and hence a POD measurement looking at the initial drop in signal will have a low value, whereas for 140° immediately following the crack there is very little signal, leading to a high POD. The B-Scan is also a visual method of implementing reflection coefficient analysis. Take for example 40° and 140°; the amplitude of the first reflection is clearly very different. Understanding B-Scans using this method requires either a trained operator, or a trained

image recognition system [27].

7. Conclusions and further work

Our 3D model for the reflection and transmission coefficients for angled defects has shown very good agreement with the experimental data, and furthermore shows good agreement with previous analytical models for an infinite length crack (wedge angle) [16, 17]. The scattering cross section confirms the physical validity of the model. It is clear that both length and angle of a surface defect needs to be considered when interpreting the results of ultrasonic measurements using Rayleigh waves.

The 3D model gives a picture of the displacements within the sample before, during, and after interaction with the crack, allowing insight into the behaviour of the waves. In particular the mode-conversion at the bottom of the crack can be investigated. Simulated B-Scans allow understanding of the transmission measurements, confirming that a near-field measurement of the peak to peak amplitude of the Rayleigh waves will give a high POD for certain angles, whereas for accurate calibration a far-field measurement of the transmission is required.

All the above effects can be used to characterise a surface-breaking defect more fully. It is clear from this work that, whilst reflected waves can still be used to locate an angled defect, a technique which relied solely on the reflected amplitude of a wave would be unreliable for gauging crack depth. Recent work has used the *transmitted* frequency content of broadband pulses to gauge the depth of a defect which is inclined normal to the sample surface [15]. Here we have shown that crack sizing using the amplitude of transmitted waves may also be less reliable if the crack angle is not known. However, we have shown that the variation in the transmission coefficient is relatively small compared to variations in the reflection coefficient, and hence considering both will give a much more reliable measure of the defect.

A scan of a sample will give several pieces of information. Firstly, the reflection can be measured, and the frequency content and multiple reflections up and down the crack analysed. Secondly, the peak to peak amplitude in the windowed expected Rayleigh wave arrival time can be measured and the transmission calculated. Finally, consideration of the shape of the wavemodes in the B-Scan can give an idea of the angle of the defect, with the position of symmetry of the wavemodes and the recovery time analysed. Machine learning for image processing may be beneficial in this case [27]. A further

input will be the enhancement in the near-field due to interactions of waves and changes in boundary conditions at the crack; these will be investigated in a further publication [18].

This work has applications in many areas of NDT. A simple angled / not angled measurement would allow discrimination between rolling contact fatigue in rails and other rail breakages, such as weld failures. It remains to be seen whether it will be useful in characterising stress corrosion cracking, where the defects grow into the sample in a branched manner. However, in this work we have shown that previous work calibrating the change in transmission for 90° cracks of different depths cannot be applied blindly; there is an angle dependence to the transmission which must be taken into account. Calibration measurements for a new technique must therefore consider both angle and length.

Acknowledgments

This work was funded by the European Research Council under grant 202735, ERC Starting Independent Researcher Grant. We also thank NESTA for Crucible Seed Funding.

References

[1] Cannon, D.F., Edel, K.-O., Grassie, S.L. and Sawley, K., Fatigue Fract Engng Mater Struct, 2003. 26 p.865-887.

[2] Blake, R.J. and L.J. Bond, Ultrasonics, 1992. 30(4): p. 255-265.

[3] Cooper, J.A., Crosbie, R.A., Dewhurst, R.J., Mckie, A.D.W. and Palmer, S.B., IEEE Transactions on Ultrasonics Ferroelectrics and Frequency Control, 1986. 33(5): p. 462-470.

[4] Hutchins, D.A., Ultrasonics, 1988. 26(4): p. 198-203.

[5] Jian, X., Dixon, S., Guo, N. and Edwards, R.S., Journal of Applied Physics, 2007. 101(6): p. 7.

[6] Arias, I. and J.D. Achenbach, Wave Motion, 2004. 39(1): p. 61-75.

[7] Dixon, S., Cann, B., Carroll, D.L., Fan, Y. and Edwards, R.S., Nondestructive Testing and Evaluation, 2008. 23(1): p. 25-34.

[8] Edwards, R.S., S. Dixon, and X. Jian, NDT & E International, 2006. 39(6): p. 468-475.

[9] Edwards, R.S., Jian, X., Fan, Y. and Dixon, S., Applied Physics Letters, 2005. 87(19): p. 3.

[10] Fan, Y., Dixon, S., Edwards, R.S. and Jian, X., NDT & E International, 2007. 40(6): p. 471-477.

[11] Jian, X., Fan, Y., Edwards, R.S. and Dixon, S., Journal of Applied Physics, 2006. 100(6): p. 6.

[12] Kinra, V.K. and Vu, B.Q., Journal of the Acoustical Society of America, 1986. 79(6): p. 1688-1692.

[13] Kromine, A.K., Fomitchov, P.A., Krishnaswamy, S. and Achenbach, J.D., Materials Evaluation, 2000. 58(2) p. 173-177.

[14] Vu, B.Q. and V.K. Kinra, Journal of the Acoustical Society of America, 1985. 77(4): p. 1425-1430.

[15] Edwards, R.S., S. Dixon, and X. Jian, Ultrasonics, 2006. 44(1): p. 93-98.

[16] Babich, V.M., Borovikov, V.A., Fradkin, L.J., Kamotski, V. and Samokish, B.A., NDT & E International, 2004. 37(2): p. 105-109.

[17] Fujii, K., Bulletin of the Seismological Society of America, 1994. 84(6): p. 1916-1924.

[18] Dutton, B., Rosli, M.H., Clough, A.R. and Edwards R.S., in preparation.

[19] Aindow, A.M., R.J. Dewhurst, and S.B. Palmer, Optics Communications, 1982. 42(2): p. 116-120.

[20] Hutchins, D.A., Canadian Journal of Physics, 1986. 64(9): p. 1247-1264.

[21] Klein, M.B., Bacher, G.D., Grunnet-Jepsen, A., Wright, D. and Moerner, W.E., Optics Communications, 1999. 162: p. 79-84.

[22] Dutton, B., Rosli, M.H. and Edwards, R.S., Review of Progress in QNDE 2010, 29A, p. 647-654.

[23] Arias, I. and J.D. Achenbach, International Journal of Solids and Structures, 2003. 40(25): p. 6917-6935.

[24] Bosseboeuf, A., Breluzeau, C., Parrain, F., Coste, P., Gilles, J.P., Megherbi, S. and Le Roux, X., SPIE-Int Soc Optical Engineering: Bellingham, 2006. p. D3451-D3451.

[25] Hirao, M. and H. Ogi, *EMATs for Science and Industry: Noncontacting Ultrasonic Measurements* 2003, Boston ; London: Kluwer Academic Publishers.

[26] Dutton, B., Boonsang, S. and Dewhurst, R.J., Sensors and Actuators A: Physical, 2006. 125(2): p. 249-259.

[27] Rosli, M.H., Edwards, R.S., Dutton, B., Johnson, C.G. and Cattani, P., Review of Progress in QNDE 2010, 29B, p. 1593-1600.